

# Cambridge Centre for Computational Chemical Engineering

University of Cambridge

Department of Chemical Engineering

Preprint

ISSN 1473 – 4273

## An aromatic site description of soot particles

Matthew Celnik, Abhijeet Raj, Richard West,

Robert Patterson, Markus Kraft\*

released: 5 November 2007

Department of Chemical Engineering  
Cambridge University  
New Museums Site  
Pembroke Street  
Cambridge CB2 3RA  
UK

\*E-mail: [mk306@cam.ac.uk](mailto:mk306@cam.ac.uk)

Preprint No. 51



**c4e**

---

*Key words and phrases:* soot, PAH, aromatic site, modelling, simulation, Monte-Carlo

**Edited by**

Cambridge Centre for Computational Chemical Engineering  
Department of Chemical Engineering  
University of Cambridge  
Cambridge CB2 3RA  
United Kingdom.

**Fax:** + 44 (0)1223 334796

**E-Mail:** [c4e@cheng.cam.ac.uk](mailto:c4e@cheng.cam.ac.uk)

**World Wide Web:** <http://www.cheng.cam.ac.uk/c4e/>

## Abstract

A new, advanced soot particle model is developed which describes soot particles by their aromatic structure including functional site descriptions and a detailed surface chemistry mechanism. A methodology is presented for the description of polyaromatic hydrocarbon (PAH) structures by their functional sites. The model is based on statistics which describe aromatic structural information in the form of easily computed correlations, which were generated using a kinetic Monte-Carlo algorithm to study the growth of single PAH molecules. A comprehensive surface reaction mechanism is presented to describe the growth and desorption of aromatic rings on PAHs. The model is capable of simulating whole particle ensembles which allows bulk properties such as soot volume fraction and number density to be found, as well as joint particle size and surface area distributions. The model is compared to the literature-standard soot model (Appel, Bockhorn and Frenklach, *Combust. Flame*, 121:122-136, 2000) in a plug-flow reactor and is shown to predict well the experimental results of soot mass, average particle size and particle size distributions at different flow times. Finally carbon/hydrogen ratio and the distribution of average PAH sizes in the ensemble, as predicted by the model, are discussed.

# Contents

<b>1</b>	<b>Introduction</b>	<b>5</b>
<b>2</b>	<b>Model</b>	<b>6</b>
2.1	Surface Processes . . . . .	7
2.2	Jump Processes . . . . .	9
<b>3</b>	<b>Kinetic Monte-Carlo Simulations</b>	<b>13</b>
<b>4</b>	<b>Site-Counting Model</b>	<b>14</b>
<b>5</b>	<b>Algorithm</b>	<b>15</b>
<b>6</b>	<b>Modelling A Plug-Flow Reactor</b>	<b>16</b>
6.1	Problem Description . . . . .	16
6.2	Results . . . . .	18
6.2.1	Bulk Properties . . . . .	18
6.2.2	Particle Size Distributions . . . . .	20
6.2.3	Carbon to Hydrogen (C/H) Ratio . . . . .	22
6.2.4	PAH Size . . . . .	25
6.2.5	Process Rates . . . . .	25
<b>7</b>	<b>Conclusions</b>	<b>27</b>

# 1 Introduction

This paper details an advanced model for soot particles. The model is developed on the assumptions that soot particles are essentially graphitic in nature and have clearly definable properties such as active surface sites. This model shall be referred to as the aromatic site soot model or ARS model.

Soot particle growth models in the past have been very simple. This was in part due to the limitations of the numerical methods used. Moment methods [9], sectional methods [27, 34] and galerkin methods [3] are very efficient algorithms, but they do not scale easily. Their complexity and computational expense scale roughly exponentially with the size of the particle type space. Hence simulations have been limited to either spherical [11] or surface-volume [24] / fractal [17] particle models with only one component: carbon. Monte-Carlo methods [4] can be easily scaled to model very complex particles [5, 23]. The focus of most model development until now has been the characterisation of soot aggregate structure rather than surface chemistry.

The soot growth model proposed by Frenklach and Wang [11] and updated by Appel et al. [2] is still the basis of most soot models used today. In this model, usually referred to as the ABF soot model, though FW model might be more appropriate, soot growth occurs through the addition of acetylene ( $C_2H_2$ ) and by the condensation of PAHs (only pyrene was considered at the time). The first fundamental assumption of the model is that the rate of acetylene addition is calculated for armchair sites [11, 18], which shall be defined later, and is originally derived from the high-pressure limit rate of acetylene addition to benzene given by Wang and Frenklach [32]. The first soot particles are incepted in their model by the dimerisation of pyrene, hence nascent soot particles have 32 carbon atoms and are assumed spherical with a diameter of 0.878 nm (assuming a graphite density of  $1.8 \text{ g/cm}^3$ ). The structure of the soot particles was never considered in this model, therefore, in order to calculate the rates, some assumptions were made about the particle surfaces. The concept of surface sites was introduced and a surface site density was estimated [11]. Frenklach and Wang [11] calculated the surface site density to be  $2.3 \times 10^{15} \text{ sites/cm}^2$  by considering the size of a benzene ring and the separation of PAH layers in soot. This is also a fundamental assumption of the model. The surface area of soot particles was calculated under the assumption that they were spherical. Subsequent work has developed this model by relaxing the sphericity assumption, for example see Patterson and Kraft [24]. However, the fundamental assumption of particle surface structure made by Frenklach and Wang [11] remained constant throughout all these studies.

There has been relatively little effort to investigate the chemical structure of soot particles. Carbon/Hydrogen ratios [6, 30] seem to be about as complex as it gets with simulating particle ensembles. At the same time a lot of work has been completed to study the morphologies of single particles [8, 14, 30, 31]. Frenklach [8] developed a detailed mechanistic model of PAH surface growth, which has been used to simulate the growth of PAH surfaces [10, 14]. Violi [30] used kinetic Monte Carlo — molecular dynamics (KMC-MD) to simulate the growth of 3D PAH structures. Violi and Izvekov [31] also attempted to model the aggregate structure of soot particles using these PAH structures by considering their interaction.

The work presented in this paper is an attempt to bridge the gap between detailed PAH structure modelling [14, 30] and soot particle population balance modelling [17] by using advanced Monte-Carlo methods. A complete model for the growth of PAHs in soot particles is presented, which is based on the work of Frenklach [8], Frenklach et al. [14]. A new particle state space is developed which allows the PAH composition and structure of soot particles to be modelled ensemble-wise for entire systems.

## 2 Model

A description of PAH surface sites was developed in order to identify a suitable data structure for the population balance model. This description was based on the following observable rules:

1. PAHs can be described by the number of surface “sites”. For filled PAHs these sites will form a closed loop around the PAH edge.
2. Each surface carbon belongs to two “sites”.
3. Each site consists of two surface carbon atoms (those available for reaction).
4. The previous points require that each site has two neighbouring sites.
5. A site can be distinguished by the total number of carbon atoms it contains. Acceptable counts are 2, 3, 4 and 5 carbon atoms.
6. Surface processes affect the reacting site and at least its two neighbouring sites.

In this nomenclature a surface carbon is one available for reaction which has a bonded H atom. Bulk carbon shall describe carbons in the graphene lattice. Figure 1 gives the nomenclature for different site types. A site with two carbon atoms is called a “free-edge” (ED), a site with three carbon atoms is called a “zig-zag” (ZZ) [8], a site with four carbon atoms is called an “armchair” (AC) [14] (also called elsewhere a “boat” site [8]) and a site with five carbon atoms shall be called a “bay” (BY). In general the addition of a ring *beside* any site increases its carbon count by one, thereby converting it into a different site. Similarly the removal of a ring will decrease the carbon count of a site by one. The exception to these rules is the addition of a ring beside a bay. Clearly adding an additional carbon to a bay generates a new ring, which in turns affects the next neighbouring site of the bay.

Frenklach et al. [14] present a mechanism by which 5-member rings migrate along PAH edges. A model for 5-member ring addition and conversion to 6-member rings is included in this study, however, 5-member rings are not modelled as part of the PAH graphitic lattice. In this paper’s nomenclature R5 denotes a 5-member ring on a zig-zag site. A zig-zag site cannot react further once occupied by a 5-member ring.

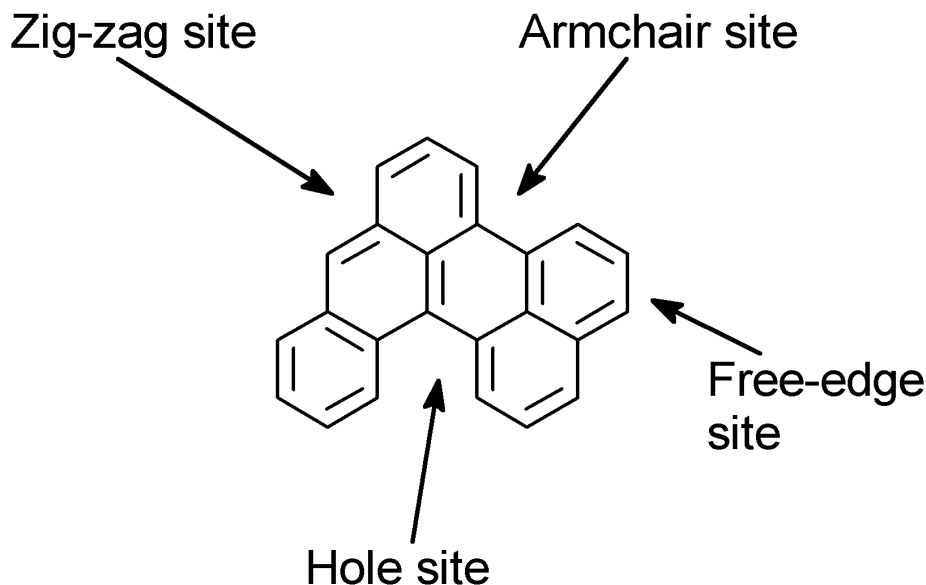


**Figure 1:** An example PAH structure showing all the different site types.

## 2.1 Surface Processes

Only hydrogen-abstraction carbon-addition (HACA) processes were considered for this work. These processes essentially proceed via the creation of surface radical sites by hydrogen abstraction, followed by the addition of acetylene to those sites. This mechanism for soot formation has been studied extensively since the early 1990s [11], and many variations on the theme have been discussed. A literature study reveals that the HACA rates are actually taken from the rates for smaller, 1 to 4 ring aromatic species; benzene (A1), naphthalene (A2), phenanthrene (A3) and pyrene (A4). The high-pressure limits of the hydrogen abstraction, acetylene addition and ring desorption reactions are taken. This is justified as processes occurring on large PAH surfaces are expected to be in the high-pressure limit. In order to develop a suitable surface chemistry mechanism an extensive literature survey was undertaken to compile the rates of all processes, along with their references. Table 1 lists all the elementary surface reactions required to create the current growth mechanism. Reactions are provided with Arrhenius rate constants and a reference to an earlier paper which describes the reaction, and which may or may not be the original source. It became apparent during this survey that there are some discrepancies in the literature for certain rates. It was not uncommon to find backward citations to rates which either did not exist or were different from those stated. Sometimes rate parameters were changed and the reasoning was not clear.

**Table 1:** PAH Surface Reactions

No.	Reaction	A	n	$E^a$	Ref.
<b>Hydrogen abstraction from free-edges, zig-zags and armchairs</b>					
1	$C_s - H + H \rightleftharpoons C_s \bullet + H_2$	$4.20 \times 10^{13}$		54.4	[8, 2]

No.	Reaction	A	n	E <sup>a</sup>	Ref.
2	$C_s^\bullet + H \rightarrow C_s$	$2.00 \times 10^{13}$		0	[2, 7]
3a	$C_s - H + OH \rightleftharpoons C_s^\bullet + H_2O$	$2.10 \times 10^{13}$		19.1	[18]
3b	$C_s - H + OH \rightleftharpoons C_s^\bullet + H_2O$	$1.60 \times 10^8$	1.42	6.1	[33]
3c	$C_s - H + OH \rightleftharpoons C_s^\bullet + H_2O$	$1.00 \times 10^{10}$	0.734	6.0	[2]
<i>Explicit reverse rates for reaction 1 from literature</i>					
-1	$C_s^\bullet + H_2 \rightarrow C_s + H$	$3.40 \times 10^9$	0.88	32.9	[8]
-1	$C_s^\bullet + H_2 \rightarrow C_s + H$	$3.90 \times 10^{12}$		39.0	[18]
-1	$C_s^\bullet + H_2 \rightarrow C_s + H$	$3.90 \times 10^{12}$		46.0	<sup>c</sup>
<b>Hydrogen abstraction from, and addition to, 5-member rings</b>					
4	$C_sR5 + H \rightleftharpoons C_sR5- + H_2$	$5.06 \times 10^7$	1.93	54.2	[14]
5	$C_sR5- + H \rightarrow C_sR5$	$6.08 \times 10^{12}$	0.27	1.2	[14]
6	$C_sR5 + H \rightleftharpoons C_sR5H-$	$8.41 \times 10^8$	1.49	4.1	[14, 26]
<b>Free-edge ring growth</b>					
7a	$C_s^\bullet + C_2H_2 \rightleftharpoons C_sC_2H_2$	$1.10 \times 10^7$	1.71	16.3	[8]
7b	$C_s^\bullet + C_2H_2 \rightleftharpoons C_sC_2H_2$	$1.10 \times 10^7$	1.71	54.2	[14]
7c	$C_s^\bullet + C_2H_2 \rightleftharpoons C_sC_2H_2$	$1.10 \times 10^7$	1.61	16.3	this work
8	$C_sC_2H_2 \rightleftharpoons C_sC_2H + H$	$4.80 \times 10^{12}$		140.3	[8, 14]
9	$C_sC_2H^\bullet + C_2H_2 \rightleftharpoons C_s(C_2H)C_2H_2$	same as reaction 7			[8, 14]
10	$C_s(C_2H)C_2H_2 \rightarrow C_sR6^\bullet$	$2.50 \times 10^{12}$	-0.13	65.7	[8, 14]
<i>Explicit reverse rate for reaction 8 from literature</i>					
-8	$C_sC_2H \rightarrow C_sC_2H_2 + H$	$1.50 \times 10^{10}$	0.85	5.0	[8]
<b>Free-edge ring desorption</b>					
11	$C_{s,ed}R6^\bullet + 2H \rightarrow C_s^\bullet + 2C_2H_2$	$1.30 \times 10^{11}$	1.08	294.6	[14]
<b>5-member ring addition to zig-zags</b>					
12	$C_s^\bullet + C_2H_2 \rightarrow C_sR5 + H$	$6.80 \times 10^{11}$		92.2	[13]
<b>5-member ring desorption</b>					
13	$C_sR5- \rightarrow C_sC_2H^\bullet$	$1.60 \times 10^{14}$		177.5	[13] <sup>b</sup>
14	$C_sC_2H^\bullet + H \rightarrow C_sC_2H$	same as reaction 2			[14]
15	$C_sC_2H + H \rightleftharpoons C_sC_2H_2$	reverse of reaction 8			[8]
16	$C_sC_2H_2 \rightarrow C_s^\bullet + C_2H_2$	$1.3 \times 10^{14}$		174.8	[8]
<b>Armchair ring growth</b>					
17	$C_s^\bullet + C_2H_2 \rightleftharpoons C_sC_2H_2$	$4.60 \times 10^6$	1.97	30.5	[8]
18	$C_sC_2H_2 \rightleftharpoons C_sC_2H + H$	$1.20 \times 10^{14}$		161.2	[8]
19	$C_sC_2H_2 \rightarrow C_sR6 + H$	$2.60 \times 10^9$	0.64	63.6	[8]
<i>Explicit reverse rates for reactions 17 &amp; 18 from literature</i>					
-17	$C_sC_2H_2 \rightarrow C_s^\bullet + C_2H_2$	$1.50 \times 10^{15}$		171.6	[8]
-18	$C_sC_2H + H \rightarrow C_sC_2H_2$	$6.70 \times 10^7$	1.67	3.8	[8]
<i>One step armchair ring growth (ABF model)</i>					
20	$C_s^\bullet + C_2H_2 \rightarrow C_sR6 + H$	$8.00 \times 10^7$	1.56	15.9	[2]
<b>5-member ring migration</b>					
21a	$C_{s,ac}R5H- \rightarrow C_sR5 + H$	$4.47 \times 10^{11}$		0	[14], 1500 K.
21b	$C_{s,ac}R5H- \rightarrow C_sR5 + H$	$1.34 \times 10^{12}$		0	[14], 2000 K.
21c	$C_{s,ac}R5H- \rightarrow C_sR5 + H$	$2.10 \times 10^{12}$		0	[14], 2300 K.
<b>5- to 6-member ring conversion at free-edges (Frenklach et al. [14])</b>					
22	$C_{s,ed}(R5H-)\bullet + C_2H_2 \rightleftharpoons C_s(R5H-)C_2H_2$	same as reaction 7			[8, 14]
23	$C_{s,ed}(R5H-)C_2H_2 \rightleftharpoons C_s(R5H-)C_2H + H$	same as reaction 8			[8, 14]
24	$C_{s,ed}(R5H-)C_2H \rightarrow C_sR6^\bullet$	same as reaction 10			[14] <sup>b</sup>
<b>5- to 6-member ring conversion at free-edges (Frenklach et al. [13])</b>					
25	$C_{s,ed}(R5)\bullet + C_2H_2 \rightleftharpoons C_s(R5)C_2H_2$	same as reaction 7			[8, 14]
26	$C_{s,ed}(R5)C_2H_2 \rightleftharpoons C_s(R5-)C_2H_3$	$1.9 \times 10^{12}$		108.4	[13]
27	$C_{s,ed}(R5-)C_2H_3 \rightleftharpoons C_s(C_2H)(C_2H_3)\bullet$	$1.6 \times 10^{14}$		177.5	[13]
28	$C_s(C_2H)(C_2H_3)\bullet \rightleftharpoons C_s(CCH_2)(C_2H_2)\bullet$	$1.8 \times 10^{13}$		230.9	[13]
29	$C_s(CCH_2)(C_2H_2)\bullet \rightleftharpoons C_s(C_2H)(C_2H_2)$	$1.0 \times 10^{13}$		19.7	[13]



No.	Reaction	A	n	E <sup>a</sup>	Ref.
30	$C_s(C_2H)(C_2H_2) \rightleftharpoons C_sR6^\bullet$	$2.6 \times 10^{11}$		41.2	[13]
<b>6- to 5-member ring conversion at free-edges</b>					
31	$C_{s,ed}R6^\bullet \rightarrow C_sR5- + C_2H_2$	$1.30 \times 10^{11}$	1.08	294.6	[14]
<b>5- to 6-member ring conversion at armchairs</b>					
32a	$C_{s,ac}R5H- \rightarrow C_sR6 + H$	$4.47 \times 10^{11}$		0	[14], 1500 K.
32b	$C_{s,ac}R5H- \rightarrow C_sR6 + H$	$1.34 \times 10^{12}$		0	[14], 2000 K.
32c	$C_{s,ac}R5H- \rightarrow C_sR6 + H$	$2.10 \times 10^{12}$		0	[14], 2300 K.
<b>Free-edge oxidation</b>					
33a	$C_sR6- + O_2 \rightarrow C_sC_2H + HCO + CO$	$2.20 \times 10^{12}$		31.4	[2]
33b	$C_sR6- + O_2 \rightarrow C_sC_2H + HCO + CO$	$2.10 \times 10^{12}$		31.3	[33]
34	$C_sR6 + OH \rightarrow C_sC_2H + CH_2CO$	$1.30 \times 10^{13}$		44.4	[33]
35	$C_sC_2H + O \rightarrow C_s^\bullet + HCCO$	$2.04 \times 10^7$	2.00	7.9	[33]
<b>Armchair oxidation</b>					
36a	$C_{s,ac}R6- + O_2 \rightarrow C_s^\bullet + 2CO$	$2.20 \times 10^{12}$		31.4	[2]
36b	$C_{s,ac}R6- + O_2 \rightarrow C_s^\bullet + 2CO$	$2.10 \times 10^{12}$		31.3	[33]
37	$C_{s,ac}R6 + OH \rightarrow C_s^\bullet + CHO + CH$	reaction probability = 0.13			[2]

<sup>a</sup>Activation energy units of  $kJ/mol$ .

<sup>b</sup>Frenklach et al. [14] assumed this to be infinitely fast.

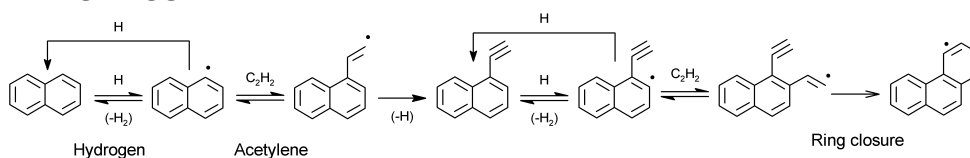
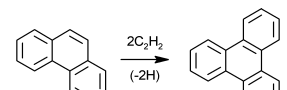
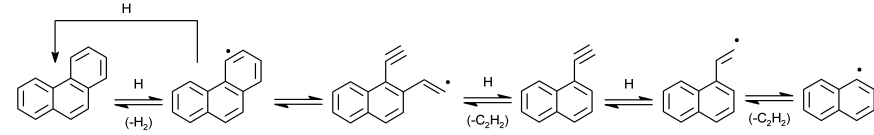
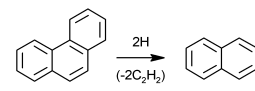
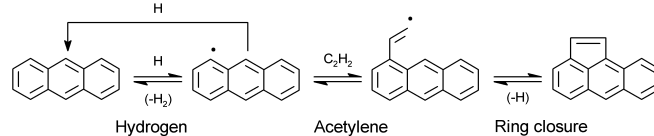
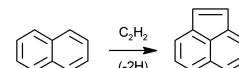
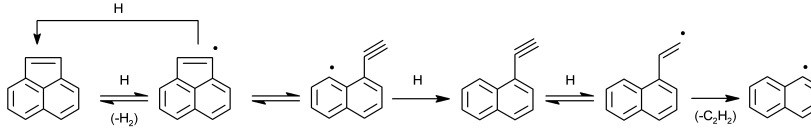
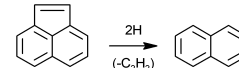
<sup>c</sup>Frenklach's MoMIC code.

The elementary reactions listed in table 1 are used to define the processes of ring growth, ring desorption and ring conversion on PAH surfaces. It is desirable to not simulate every hydrogen abstraction and acetylene addition reaction individually as the computational expense would become prohibitive. Instead the common assumption of steady-state for radical surface sites and short-lived intermediates is made [12]. In order to obtain overall rates for ring addition processes the additional assumption is made that the acetylene addition, ring closure and ring breakage processes are all irreversible. In this way it is possible to derive a rate expression for single-step jump processes. These simplified jumps form a computationally feasible mechanism, which is then solved using a Markov jump process defined in a subsequent section.

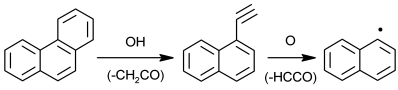
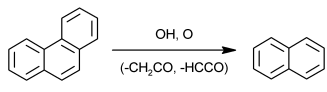
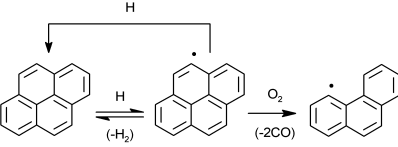
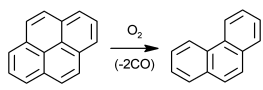
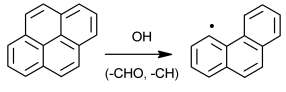
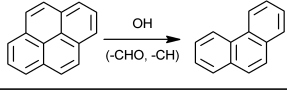
## 2.2 Jump Processes

The PAH growth processes identified from the literature [14] are listed in table 2. The complete mechanism for each process is illustrated, along with the corresponding jump process and the rate expression, based on the reactions in table 1. Frenklach et al. [14] gave all the single-step chemical processes which make up the Monte-Carlo events. Their work references an earlier paper by Frenklach [8], in which the steady-state analysis is partially discussed. Here the rate expressions obtained by applying the steady-state assumption are presented in order that subsequent researchers may easily use and check them. It is believed that this is the first time the complete chemical processes are presented alongside the corresponding jump processes, and it is hoped that this will be a useful reference in future.

**Table 2: Monte-Carlo Jump Processes**

Process	Ref.
<p><b>S1 Free-edge ring growth</b></p>  <p>Hydrogen abstraction      Acetylene addition      Ring closure</p> <p>Jump Process:</p>  <p>Rate:</p> $k_7 \left( \frac{k_1[\text{H}] + k_3[\text{OH}]}{k_{-1}[\text{H}_2] + k_2[\text{H}] + k_{-3}[\text{H}_2\text{O}] + k_7[\text{C}_2\text{H}_2]} \right) [\text{C}_2\text{H}_2][\text{C}_{\text{ed}}]$	[8]
<p><b>S2 Free-edge ring desorption</b></p>  <p>Hydrogen abstraction      Acetylene addition      Ring closure</p> <p>Jump Process:</p>  <p>Rate:</p> $k_{11} \left( \frac{k_1[\text{H}] + k_3[\text{OH}]}{k_{-1}[\text{H}_2] + k_2[\text{H}] + k_{-3}[\text{H}_2\text{O}] + k_{11}} \right) [\text{C}_{\text{ed}}\text{R6}]$	[8]
<p><b>S3 5-member ring addition</b></p>  <p>Hydrogen abstraction      Acetylene addition      Ring closure</p> <p>Jump Process:</p>  <p>Rate:</p> $k_{12} \left( \frac{k_1[\text{H}] + k_3[\text{OH}]}{k_{-1}[\text{H}_2] + k_2[\text{H}] + k_{-3}[\text{H}_2\text{O}] + k_{12}[\text{C}_2\text{H}_2]} \right) [\text{C}_2\text{H}_2][\text{C}_{\text{zz}}]$	[13]
<p><b>S4 5-member ring desorption</b></p>  <p>Hydrogen abstraction      Acetylene addition      Ring closure</p> <p>Jump Process:</p>  <p>Rate:</p> $k_{13} \left( \frac{k_4[\text{H}]}{k_{-4}[\text{H}_2] + k_5[\text{H}] + k_{13}} \right) [\text{C}_{\text{zz}}\text{R5}]$	[13]

Process	Ref.
<p><b>S5 Armchair ring growth</b> [2]</p> <p>Hydrogen abstraction      Acetylene addition      Ring closure</p> <p>Jump Process: </p> <p>Rate: <math>k_{20} \left( \frac{k_1[\text{H}] + k_3[\text{OH}]}{k_{-1}[\text{H}_2] + k_2[\text{H}] + k_{-3}[\text{H}_2\text{O}] + k_{20}[\text{C}_2\text{H}_2]} \right) [\text{C}_2\text{H}_2][\text{C}_{\text{ac}}]</math></p>	[2]
<p><b>S6 5- to 6-member ring conversion at free edge</b> [14]</p> <p>Jump Process: </p> <p>Rate: <math>k_7 \left( \frac{k_6[\text{H}]}{k_{-6} + k_{10}} \right) \left( \frac{k_1[\text{H}] + k_3[\text{OH}]}{k_{-1}[\text{H}_2] + k_2[\text{H}] + k_{-3}[\text{H}_2\text{O}] + k_7[\text{C}_2\text{H}_2]} \right) [\text{C}_2\text{H}_2][\text{C}_{\text{edR5}}]</math></p>	[14]
<p><b>S7 6- to 5-member ring conversion at free edge</b> [14]</p> <p>Jump Process: </p> <p>Rate: <math>k_{31} \left( \frac{k_1[\text{H}] + k_3[\text{OH}]}{k_{-1}[\text{H}_2] + k_2[\text{H}] + k_{-3}[\text{H}_2\text{O}] + k_{31}} \right) [\text{C}_{\text{ac}}\text{C}_{\text{edR6}}]</math></p>	[14]
<p><b>S8 5- to 6-member ring conversion at armchair</b> [14]</p> <p>Jump Process: </p> <p>Rate: <math>k_{32} \left( \frac{k_6[\text{H}]}{k_{-6} + k_{32}} \right) [\text{C}_{\text{ac}}\text{R5}]</math></p>	[14]
<p><b>S9 Free-edge oxidation by O<sub>2</sub></b> [33]</p> <p>Jump Process: </p> <p>Rate: <math>k_{33} \left( \frac{k_1[\text{H}] + k_3[\text{OH}]}{k_{-1}[\text{H}_2] + k_2[\text{H}] + k_{-3}[\text{H}_2\text{O}] + k_{33}[\text{O}_2]} \right) [\text{O}_2][\text{C}_{\text{edR6}}]</math></p>	[33]

Process	Ref.
<p><b>S10 Free-edge oxidation by OH</b></p>  <p>Jump Process:</p>  <p>Rate:</p> $k_{34}[\text{OH}][\text{C}_{\text{edR6}}]$	[33]
<p><b>S11 Armchair oxidation by O<sub>2</sub></b></p>  <p>Jump Process:</p>  <p>Rate:</p> $k_{36} \left( \frac{k_1[\text{H}] + k_3[\text{OH}]}{k_{-1}[\text{H}_2] + k_2[\text{H}] + k_{-3}[\text{H}_2\text{O}] + k_{36}[\text{O}_2]} \right) [\text{O}_2][\text{C}_{\text{ed}}]$	[33]
<p><b>S12 Armchair oxidation by OH</b></p>  <p>Jump Process:</p>  <p>Rate:</p> $2.17 \times 10^{26} T^{0.5} [\text{OH}] d_{\text{col}}(x)$	[33]

The oxidation processes listed in table 2 are based on the analogous gas-phase reactions for naphthalene (A2), phenanthrene (A3) and pyrene (A4) given by Wang and Frenklach [33]. As in the ABF model pyrene condensation was the only condensation processes considered. Pyrene condensation was modelled as a free molecular collision between the pyrene molecule and the soot particle [28].

The PAH site and combined-site concentrations which appear in table 2 are derived from the site types shown in figure 1. They are summarised here:

1.  $[\text{C}_{\text{ed}}]$  is the concentration of free-edges sites.
2.  $[\text{C}_{\text{edR6}}]$  is the concentration of 6-member rings on free-edge sites.
3.  $[\text{C}_{\text{zz}}]$  is the concentration of zig-zag sites.
4.  $[\text{C}_{\text{zzR5}}]$  is the concentration of 5-member rings on zig-zag sites.
5.  $[\text{C}_{\text{ac}}]$  is the concentration of armchair sites.
6.  $[\text{C}_{\text{edR5}}]$  is the concentration of 5-member rings which are *adjacent* to free-edge sites.

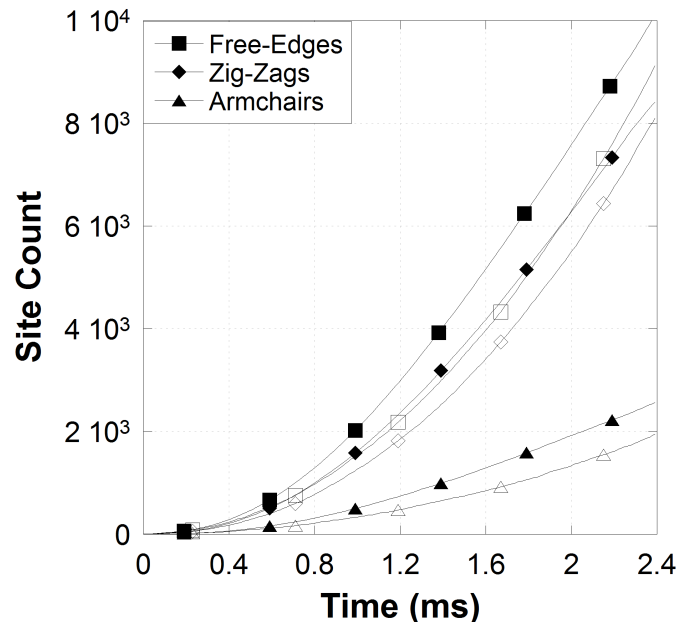


**Figure 2:** Comparison of full PAH structure KMC results to the site-counting model. Solid symbols are site-counting model, open symbols are KMC simulations.

7.  $[C_{ac}R5]$  is the concentration of 5-member rings which are *adjacent* to armchair sites.
8.  $[C_{ac}C_{ed}R6]$  is the concentration of armchair sites which are *adjacent* to three consecutive free-edge sites (a 6-member ring).

It is important to note that some of these expressions involve multiples of the surface sites identified in figure 1.

### 3 Kinetic Monte-Carlo Simulations

A 2D PAH structure kinetic Monte-Carlo (KMC) code was developed which simulates the evolution of single PAH molecules in a gas-phase environment. In the long term it is expected that this code will be integrated into the stochastic particle model, however, the computational expense of simulating thousands of growing PAHs would be very large. This code was used to generate statistics of combined-site concentrations, as used in table 2, as functions of the basic surface site types. These statistics were used in the site counting model described below. There are three areas in which the information generated by this KMC code can influence the site counting model. The first is the generation of correlation of combined-sites, second the probability of neighbouring site types can be evaluated, and third the fraction of sites which may be sterically unavailable can be found. These areas shall be discussed in the next section.

Figure 2 demonstrates the agreement capable between the KMC simulations and the site-counting model. The agreement is reasonable given the assumption made in order to formulate the site-counting model, and is probably sufficient to justify the use of the site-

counting model. Discussion of the statistics generated by the KMC code shall be given in a further paper

## 4 Site-Counting Model

The site-counting model describes the aromatic structure of soot particles with only nine variables, thereby allowing complete particle systems to be simulated relatively quickly. It represents the bridge between kinetic Monte-Carlo or molecular dynamics and the simple spherical carbon soot particle models. The site-counting model tracks the number of each site type per particle while neglecting the relative positions of the sites. The composition of the soot particles is tracked by counting the number of carbon and hydrogen atoms [6]. An approximation of the aggregate structure is obtained by using the surface-volume model [24]. Hence, the particles occupy a nine dimensional state space given by

$$E = (C, H, N_{ed}, N_{zz}, N_{ac}, N_{bay}, N_{R5}, S_a, N_{PAH})$$

where  $N_x$  is the number of site type  $x$ ,  $C$  and  $H$  are the number of carbon and hydrogen atoms respectively,  $S_a$  is the surface area of the particle and  $N_{PAH}$  is the number of PAHs which make up the particle. The motivation of this model was to produce as much information about the PAH structure of soot as possible, while keeping the computational expense low enough to simulate particle populations, rather than just single particles.

The PAH KMC code described above was used to provide information about PAH structure which was then implemented in the site counting model. In the site-counting model the values of  $[C_{ed}R6]$ ,  $[C_{ed}R5]$ ,  $[C_{ac}R5]$  and  $[C_{ac}C_{ed}R6]$  are approximations only. Estimates of these values were obtained by developing a linear correlation with a single known quantity. The concentrations  $[C_{ed}R6]$ ,  $[C_{ed}R5]$  and  $[C_{ac}C_{ed}R6]$  are functions of the number of free-edges, and  $[C_{ac}R5]$  is a function of the number of armchairs. The linear correlations were developed by simulating the 2D structural evolution of a few PAH molecules in a fixed chemical environment at different temperatures in the range 1500 K to 2000 K using the KMC code. While such correlations may not be ideal, statistical studies of PAH structures are essentially non-existent, so they should give a reasonable first approximation. It is intended to perform an in-depth study on this topic at a future point. The correlations for these four quantities are given here:

$$[C_{ed}R6] = [4.43 \times 10^{-2} + (0.102[C_{ed}])] \quad (1)$$

$$[C_{ed}R5] = [0.374 + (3.62 \times 10^{-3}[C_{ed}])] \quad (2)$$

$$[C_{ac}C_{ed}R6] = [0.648 + (2.94 \times 10^{-3}[C_{ed}])] \quad (3)$$

$$[C_{ac}R5] = [-8.58 \times 10^{-3} + (1.99 \times 10^{-2}[C_{ac}])] \quad (4)$$

Each process listed in table 2 must change the particle state space in a clearly defined way. The state space changes were formulated by consideration of the underlying physical processes and consideration of PAH sites discussed earlier. The particle state changes are given in table 3.

When a ring is added or desorbed from a PAH site it necessarily changes the structure of the PAH surface. Each site has two neighbouring sites, which must both be updated. In general, ring addition increases the number of carbon atoms in the neighbouring sites by one each (incrementing), and ring desorption decreases the number of carbon atoms by one each (decrementing). This change to the neighbouring site types occurs according to the rules in table 5. It was realised that not all site configurations are equally likely, which means that not all sites are equally probable to be neighbours of a reacting site. In order to correctly select neighbouring sites a further study was conducted using the 2D PAH KMC code. For each process the current state of the PAH molecule, as it applies in the site counting model, was stored. The neighbours of the site selected for reaction were noted. The code was run several times at different temperature and for different molecules, to provide a large data set of reaction events and the corresponding neighbouring sites. This allowed the probability distribution of the neighbouring sites to be found. The neighbour weight distributions for each process are listed in table 4. These weights are multiplied by the number of the relevant site to calculate effective site concentrations, which are then used to randomly select a neighbour.

Bay sites present a problem in this representation as addition of a carbon atom to a bay should complete a new 6-member ring, which in turn affects the next neighbour to the bay. If this next neighbour is also a bay, then a further site must be considered and so on. In this way, for certain PAH structures, one acetylene addition could complete several rings, though thermodynamics might dictate that such structures should not exist, or at least would be very unstable. For the site-counting model, as a first approximation, the incrementing of bays was ignored, and when a bay was chosen for incrementing it was just deleted and no further action was taken. This may be justified as it is expected that the concentration of bays relative to other sites should be small. Activity around bays, and interaction of hydrogen atoms in particular, is highlighted as an area which requires additional research.

## 5 Algorithm

The ARS and site-counting models were integrated into a multivariate population balance model, solved using a Monte-Carlo technique, which was then used to simulate soot formation. A stochastic particle is described by the following variables: carbon atom count, hydrogen atom count, free-edge site count, zig-zag site count, armchair site count, R5 site count, hole site count and surface area. By tracking surface area as well as carbon atom count, an approximation of the aggregate structure of the particle can be modelled. The model is formulated in terms of a particle type space, for which jump transformation and rates are defined. These can then be solved using DSMC. Table 3 shows the state change of a stochastic particle due to each Monte-Carlo surface event considered. Most surface events require further sites to be updated, because processes affect the neighbouring sites

of the reacting site. When choosing neighbouring sites to be updated, R5 sites were not considered because the governing process could not have occurred were the R5 present.

Once a process has been selected using the Monte-Carlo algorithm [4], a particle is selected and updated. The algorithm for updating particles for the processes listed in table 3 is written here and given as a flowchart in figure 3:

1. Where table 3 requires sites to be subtracted for the process, subtract those sites.
2. If process is a ring growth (except R5 addition) then select neighbouring site, using the weights in table 4, to increment from free-edges, zig-zags, armchairs and bays.
3. If process is a desorption or oxidation (except R5 desorption) then select neighbouring site, using the weights in table 4, to decrement from zig-zags, armchairs and bays.
4. Increment/decrement neighbouring site using the rules in table 5.
5. If updated required number of neighbouring sites, then continue, else go to step 2.
6. Where table 3 requires sites to be added for the process, add those sites.
7. Update  $C$ ,  $H$  and  $N_{PAH}$  using the rules defined for the current process in table 3.

It is important to first subtract sites when a process requires it (step 1) in order that those sites are not selected for incrementing/decrementing. Addition of sites by a process must be performed after updating neighbouring sites for the same reason.

## 6 Modelling A Plug-Flow Reactor

The experimental plug-flow reactor (PFR) studies of Kronholm and Howard [19], Marr [22] were used to validate the model. This study has previously been simulated by Celnik et al. [6], Wen et al. [34]. The apparatus consists of a jet-stirred reactor (JSR) feeding a tube section which gives an approximation to plug-flow. Wen et al. [34] have used the experimental results of Kronholm and Howard [19], Marr [22] to validate a model solved using a moving sectional method and to compare different variations of the ABF soot growth model. The aromatic site (ARS) model is compared to the ABF model and the experimental results. The different soot-growth and particle models are compared by considering the time evolution of the particle C/H ratios and by considering the predicted process rates.

### 6.1 Problem Description

The simulation of the JSR and PFR were as described by Celnik et al. [6], and it is discussed here for completeness. The JSR was solved using gas-phase chemistry equations only, as neither Kronholm nor any of the preceding work mentions soot particles in the



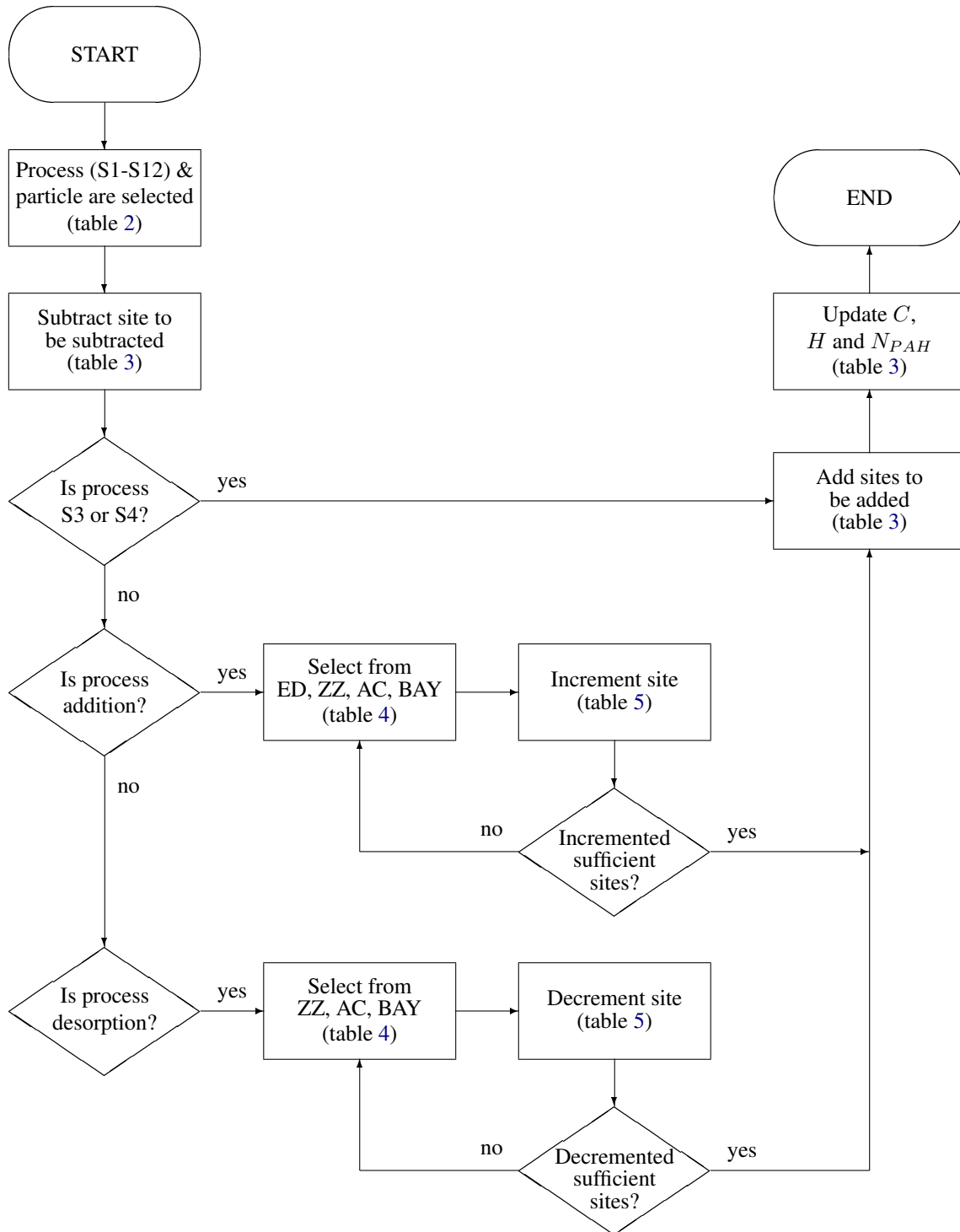


**Figure 3:** Algorithm for updating particle state space once a process has been chosen

JSR. Solution of the JSR therefore is a simple matter of solving the gas-phase material balances using a standard ODE solver. DDASSL was used in this case. The JSR feed was a  $C_2H_2$ /Air mixture with equivalence ratio 2.2. The pressure and temperature were constant at 1 atm and 1630 K respectively. The residence time of the JSR was 5.7 ms [21]. The JSR was solved for a sufficiently long time period so that the solution reached steady-state. The final conditions in the JSR were then used as inputs to the coupled soot and chemistry solver for the PFR.

The PFR pressure (constant) and initial temperature were 1 atm and 1620 K respectively, and it was solved using the adiabatic energy equation, which, consistent with observations quoted by Wen et al. [34], predicted a temperature rise of 90 K through the reactor. The PFR was simulated using a maximum of 4096 stochastic particles, 20 runs and 100 steps per millisecond of flow time.

The surface-volume model of Patterson and Kraft [24] was used to provide a description of particle aggregate structure. The ARS model is compared to the ABF model predictions which were reported by Celnik et al. [6].

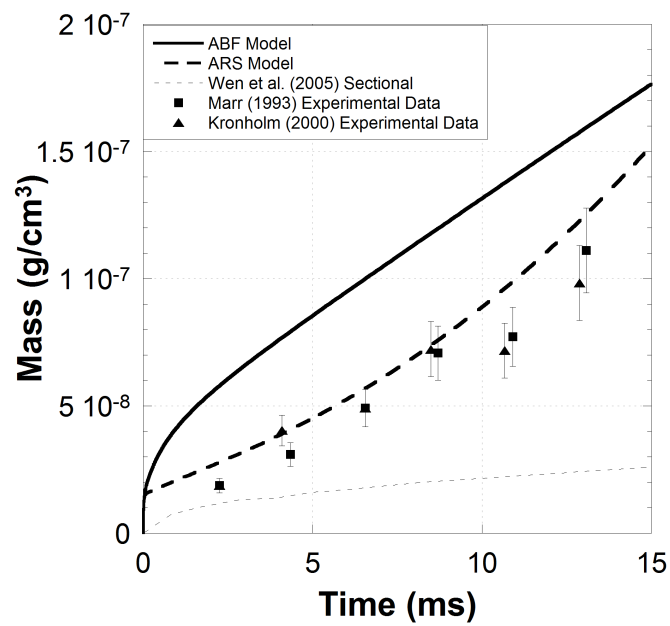
## 6.2 Results

### 6.2.1 Bulk Properties

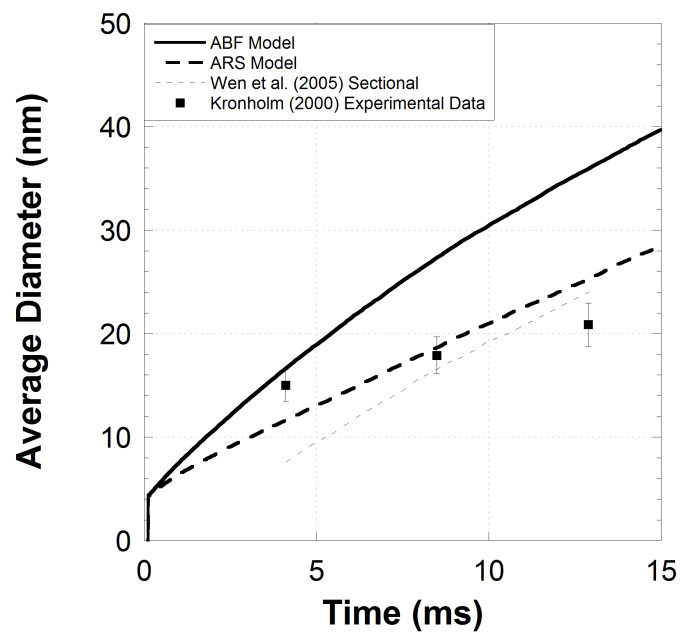
Quantities of interest have been plotted along with the experimental results of Kronholm taken from Kronholm [20], Kronholm and Howard [19] and the sectional method simulation of Wen et al. [34].

Figure 4 shows the prediction of total soot mass concentration using different models compared to the experimental data. The ARS model shows a better fit to the experimental data, however, the prediction was found to be very sensitive to the rate constants used for free-edge growth, therefore without an estimate of the error in their reported values it is difficult to draw firm conclusions from this. Model “3” by Wen et al. [34] is equivalent to the ABF soot model but for spherical particles using a sectional technique. The difference between the predictions of Wen et al. [34] and those given here may be due to their use of a constant temperature model and a different soot particle description, whereas we used an adiabatic model. Both soot model curves may predict the correct shape compared to the experimental data, however it is difficult to judge due to the relatively few experimental data points.

Figure 5 shows the average particle diameter for all particle models compared to the experimental results and simulations by Wen et al. [34]. As discussed by Celnik et al. [6] it is very possible that very small particles were not measured by the experimental technique, therefore this figure shows the average diameter calculated by neglecting all particles under 4 nm in diameter. The ABF model overpredicts the average particle diameter by up to 15 nm, yet agrees well with the simulations of Wen et al. [34] in terms of gradient. The ARS model is a better match to the experimental data than the ABF model. The ARS model almost matches the sectional simulations, which used the ABF model, and is the best fit to the experimental data of all considered model combinations.



**Figure 4:** Soot mass concentration in PFR compared to experimental data and sectional method simulations of Wen et al. [34].



**Figure 5:** Average particle diameter in PFR compared to experimental data and sectional method simulations of Wen et al. [34]. Particles with diameters smaller than 4 nm were neglected from average.

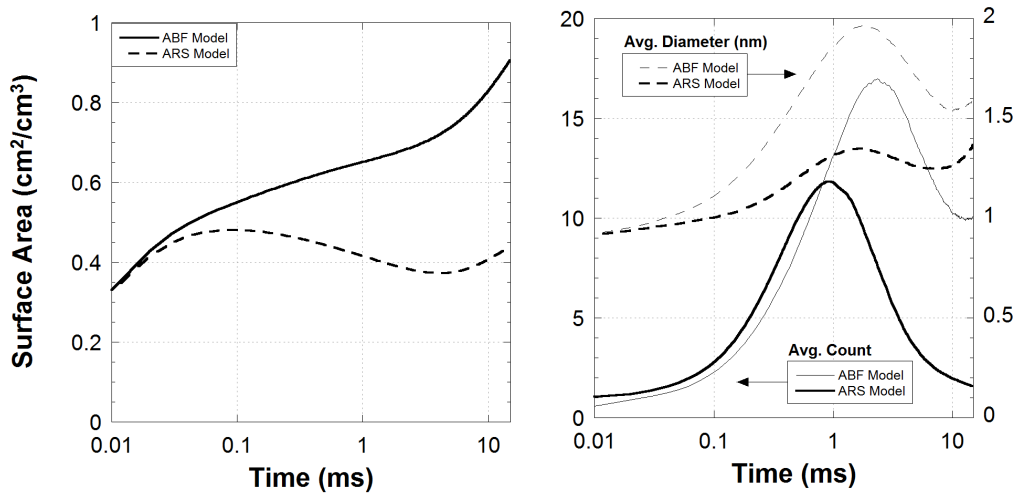


**Figure 6:** Predicted soot surface area in PFR for all particle models.

The total soot surface area per unit volume is shown in figure 6. The ABF model process rates are dependent on surface area, which is not the case for the ARS model, therefore the feedback observed for the ABF model is not observed for the ARS model. This might explain why the ABF mode predicts significantly more soot surface area than the ARS model (left plot). The lower surface area also suggests that the ARS model predicts particles of greater sphericity than the ABF model. The right plot shows the predicted primary particle counts and diameters for both models. It is evident from this figure that the ARS model predicts fewer primary particles, which agrees with the supposition of more spherical particles. The ARS model also predicts smaller primary particles, which supports the smaller mean particle diameter observed in figure 5.

### 6.2.2 Particle Size Distributions

The experimental data of Kronholm [20], Kronholm and Howard [19] is particularly useful for model validation as it includes particles size distributions (PSDs) at different flow times. These shall be discussed here. Figures 7 to 9 show the predicted PSDs and the experimental PSDs at 7.6 ms, 12.0 ms and 16.4 ms flow times consecutively. All the predicted PSDs demonstrate bimodality with a substantial quantity of fine particles. The trough between the peaks occurs in the range 5-8 nm for all plots. This somewhat justifies the decision to neglect particles smaller than 4 nm when calculating the mean particles diameter (figure 5).

Both models are poor at predicting the second peak height, the prediction gets gradually worse with flow time until there is more than an order of magnitude difference. Both models predict a broader second peak than the experimental data. This results in the greater

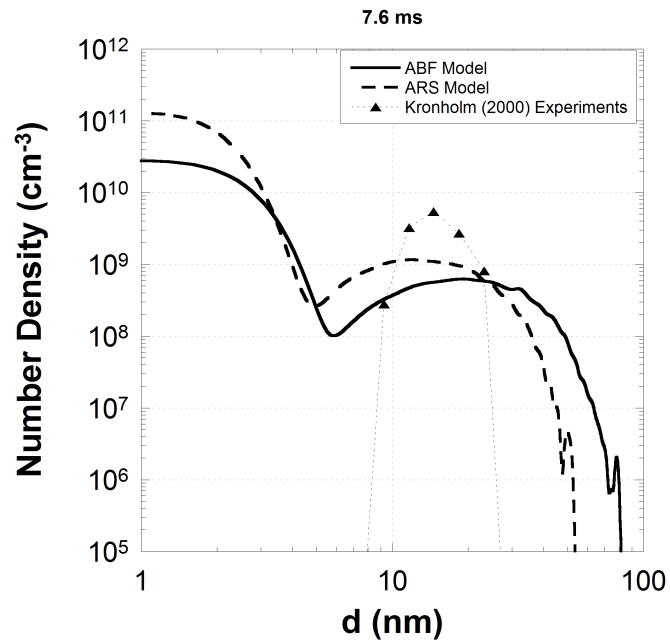


**Figure 7:** Predicted particle size distributions in PFR compared to experimental data at 7.6 ms flow time.

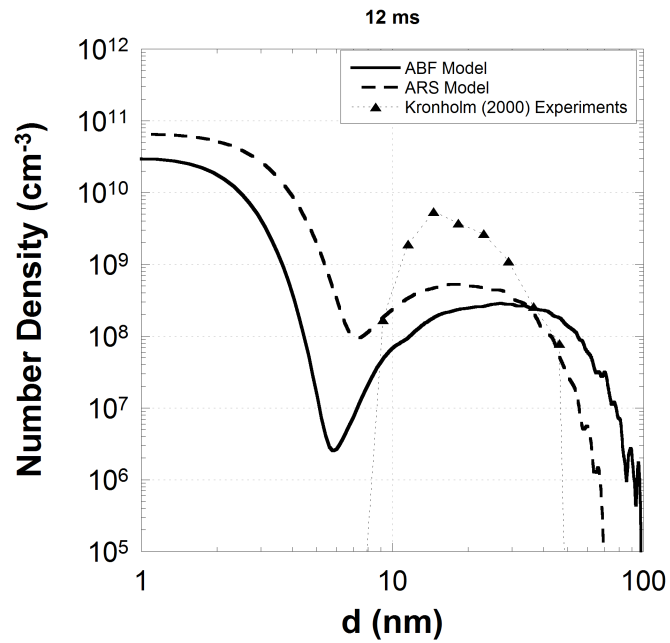


**Figure 8:** Predicted particle size distributions in PFR compared to experimental data at 12.0 ms flow time.

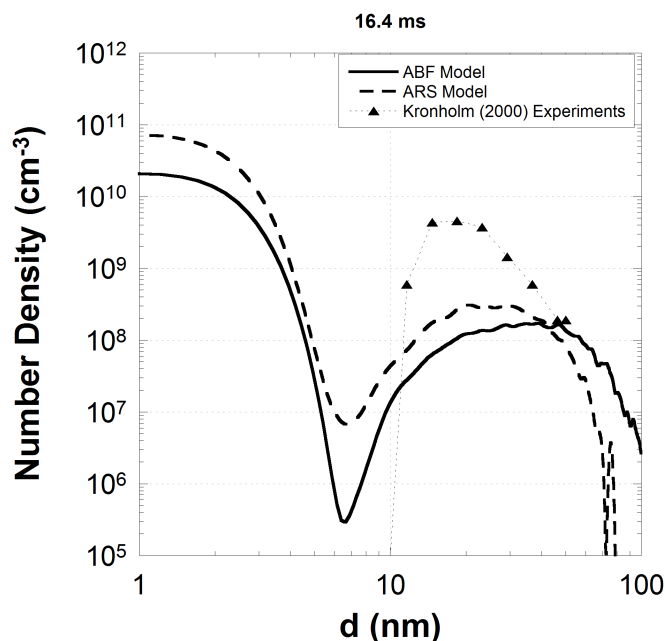


**Figure 9:** Predicted particle size distributions in PFR compared to experimental data at 16.4 ms flow time.

mean particle diameter observed in figure 5 for the ABF model. The ABF model predicts that the second peak occurs at a greater particle size than the ARS model, and it also over-predicts the second peak diameter compared to the experimental data. However, the ARS model is generally in good agreement with the experimental data. The predicted diameter at which the second peak maximum occurs is very close to the experimental result. This agreement is not diminished at different flow times. The ARS model also predicts a larger peak number density than the ABF model, which makes it a more appropriate fit to the experimental data, if not a precise fit.

### 6.2.3 Carbon to Hydrogen (C/H) Ratio

Unlike the other techniques, the stochastic technique allows the composition of the particulate matter to be tracked explicitly at limited additional computational cost. Figures 10 and 11 show the carbon to hydrogen (C/H) ratio of each particle plotted against particle diameter as scatter plots. A time-series of plots is presented to illustrate how the C/H distribution changes over time. All plots demonstrate the evolution from unimodality at early times to bimodality at later times. C/H ratios are observed in the range 1-2.

For the ABF model (fig 10) the two main growth processes are  $C_2H_2$  addition and pyrene condensation. For true armchair growth  $C_2H_2$  adds in the ratio 2:0, however, the ABF model only uses the armchair growth rate to approximate all  $C_2H_2$  additions. Therefore the approximation that  $C_2H_2$  adds carbon and hydrogen in the ratio 2:1 was made. Pyrene condensation adds in the ratio 1.6:1, therefore it would be expected to observe particle compositions between these two values. This is exactly what we see from these figures.

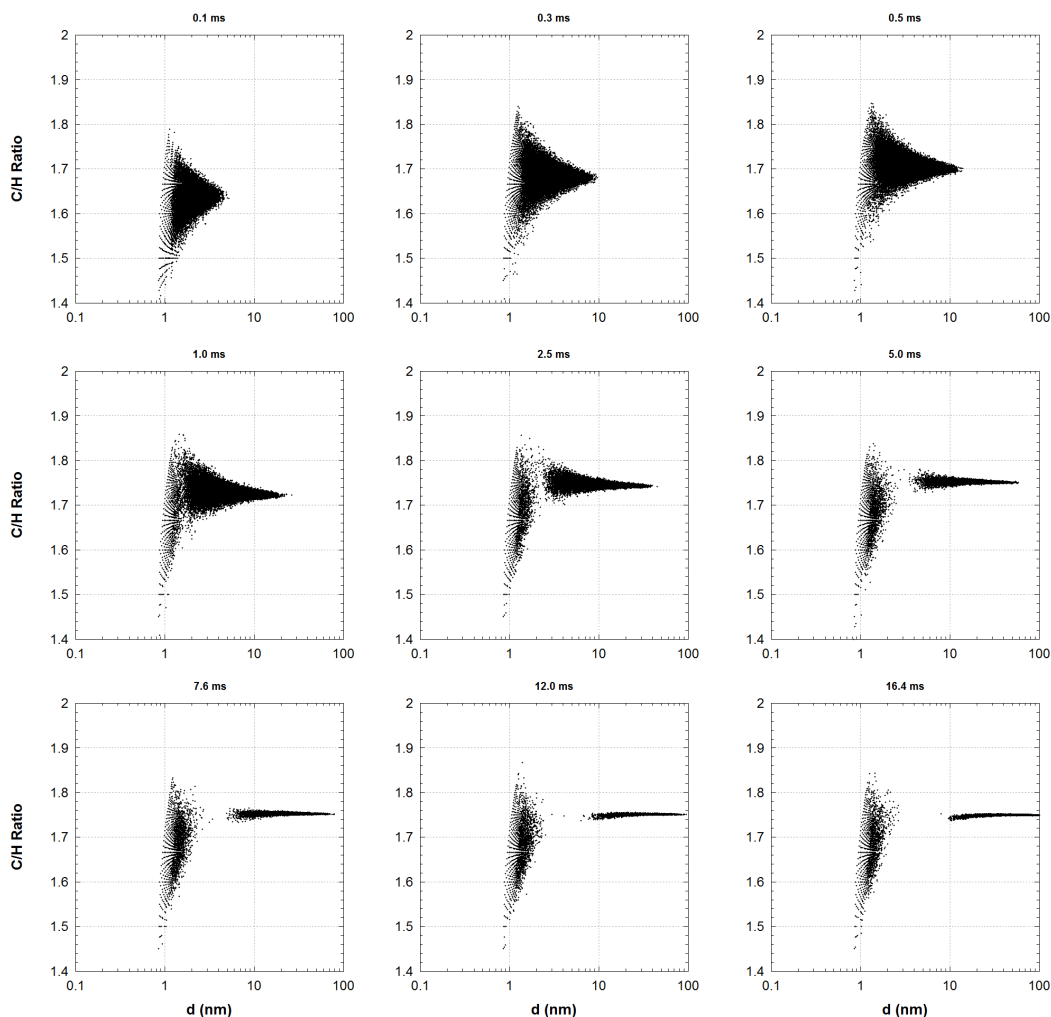


**Figure 10:** Time series C/H ratio scatter plots for the ABF soot model in PFR.

Initially the C/H ratio increases slowly suggesting that the HACA mechanism becomes dominant over condensation and inception. Larger particles show a narrower range of compositions. This is because surface processes do not alter the number of carbon and hydrogen atoms greatly relative to the total number in larger particles, for example a spherical particle of diameter 60 nm will contain over ten million carbon atoms. The model predicts a ratio around 1.75, which may be a result of the fractal nature of surface-volume particles providing more surface area per volume, thereby increasing the rate of acetylene addition in preference to pyrene condensation.

Figure 11 show C/H ratios predicted by the ARS model. For small particles the C/H ratio distributions appear very similar to those predicted by the ABF model. In fact there is little difference between the models as the smallest particles will not have much aggregate structure. C/H ratios are predicted in the range 1.95-2 as opposed to 1.9-1.95. This ratio is

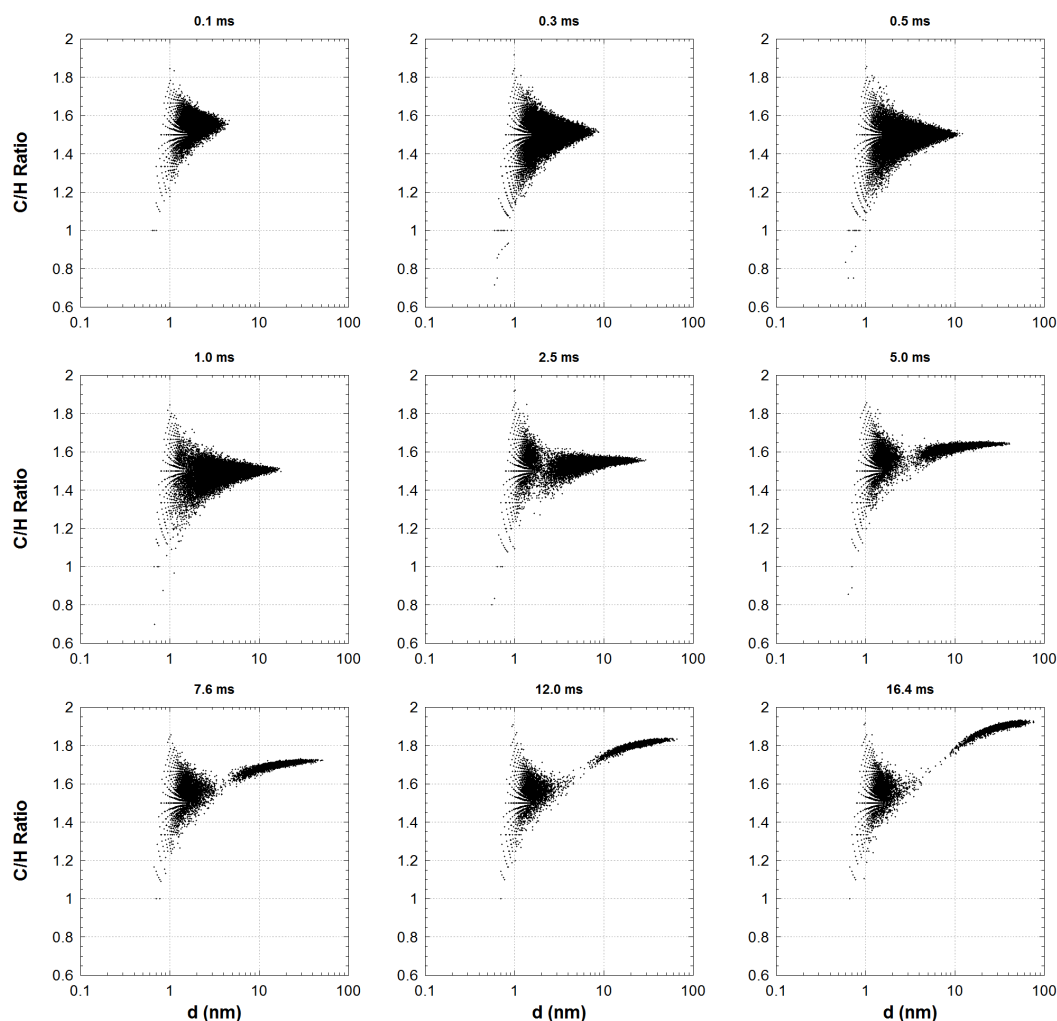


**Figure 11:** Time series  $C/H$  ratio scatter plots for the ARS soot model in PFR.

greater than that predicted by the ABF model. There is also a broader  $C/H$  ratio for larger particles than predicted by the ABF model.

The  $C/H$  ratios predicted here are consistent with young soot particles [30]. However, particles approaching 100 nm in diameter cannot realistically be called young soot, and far higher  $C/H$  ratios are reported in the literature for flame experiments, for example Harris and Weiner [15] show a ratio around 7, and Homann [16] shows a ratio greater than 10. The increase in  $C/H$  ratios at later times may be a result of graphitisation of the particles, which process has not been considered in this mechanism. It is difficult to see how a greater  $C/H$  ratio could be predicted unless additional growth species (for example alkynes) are considered or a graphitisation process is included. This is highlighted as an area which requires further work.

When considering the data on  $C/H$  ratios it is important to bear in mind the limitations of



the soot chemistry model. The ABF model considers exclusively pyrene based inception, HACA and a kinetic OH oxidation model, but soot chemistry is an active and important area of research, for examples see [27, 1]. New models, such as the ARS model, in which H and C are added in different proportions will obviously suggest different results, which will have to be evaluated now that computations are possible.

#### 6.2.4 PAH Size

The ARS site counting model tracks the number of PAHs in each computational particle as well as the number of carbon atoms. This allows the average PAH size to be found. Figure 12 shows density plots at different flow times of the average PAH size correlated against particle diameter. The shape of the plots is similar to the C/H ratio plots shown previously. This is unsurprising as larger PAH do have larger C/H ratios. The evolution of the PSD bimodality is also observed. All plot show that the smaller particles in the range 1-5 nm consist mainly of PAHs of between 10 and 20 carbon atoms. Pyrene, which is the only gas-phase PAH which is involved on soot processes, has 16 carbon atoms. Therefore early oxidation and surface growth account for such particles. As the particles grow so does the average PAH size, which approaches 50 atoms for 30-100 nm particles. Assuming that the unit cell of an infinite PAH has a surface area of  $0.03 \text{ nm}^2$ , this relates approximately to a PAH characteristic length of 1.23 nm, though this will be a slight under-estimate due to the assumption of an infinite PAH.

The average PAH size distribution at 16.4 ms for the larger particles is plotted in figure 13 (right plot). The left plot shows representative experimental data from a premixed acetylene flame by Vander Wal and Tomasek [29]. Their data show the fringe length (associated with PAH size) distribution for a single particle. A peak fringe length around 0.8-0.9 nm is observed, which is of the order of pyrene or coronene. This data cannot be compared directly to the simulation predictions because of the difference in the systems, however, a qualitative comparison can be made. The peak diameter is observable around 1.2 nm (around 30-50 carbon atoms) which is associated with the larger particles by figure 12. These peaks agree well with the data presented by Vander Wal and Tomasek [29], however, the tail of larger diameters shown in the left plot is not predicted by the simulations. This might be because only an average PAH size has been calculated for each particle and a distribution generated for all particles, whereas the experimental data shows statistics for a single particle only. However, it may be reasonable to assume that the average over the ensemble should resemble the average within a particle if the particle contains a sufficient large number of PAHs.

#### 6.2.5 Process Rates

Figure 14 shows the surface concentration of different PAH sites. The bold line shows a site density of  $2.3 \times 10^{15} \text{ cm}^{-2}$ , which is the assumed value used for the ABF model [2]. It is observed that the particles are dominated by free-edges and zig-zags according to the site counting model. This is qualitatively what was observed with the KMC code. This suggests that the classic armchair structure assumption, which forms the basis of the ABF soot growth mechanism is incomplete. This was also suggested by Frenklach et al.

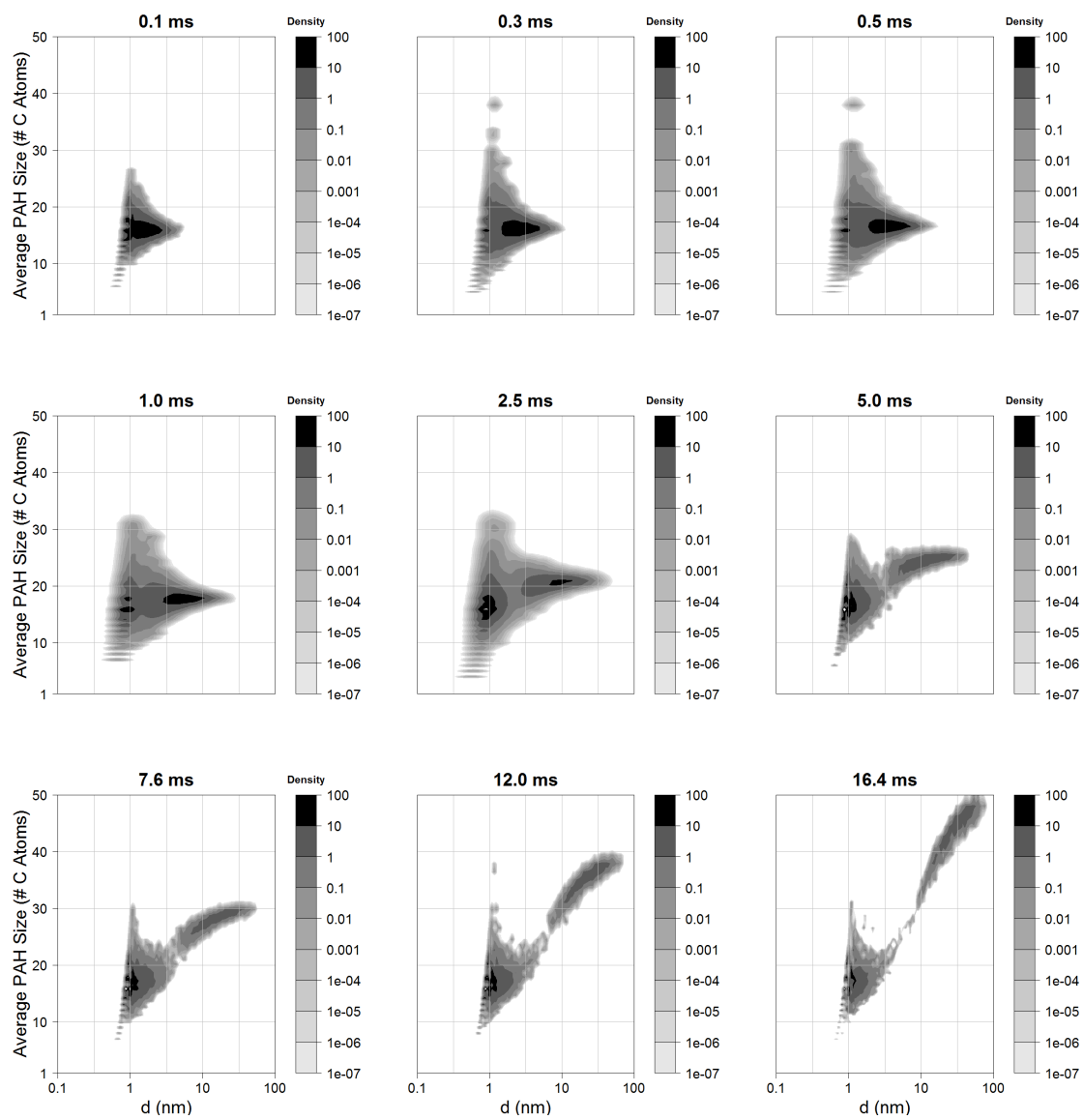


**Figure 12:** Average PAH size vs. particle diameter density plots at different flow times for the ARS model.

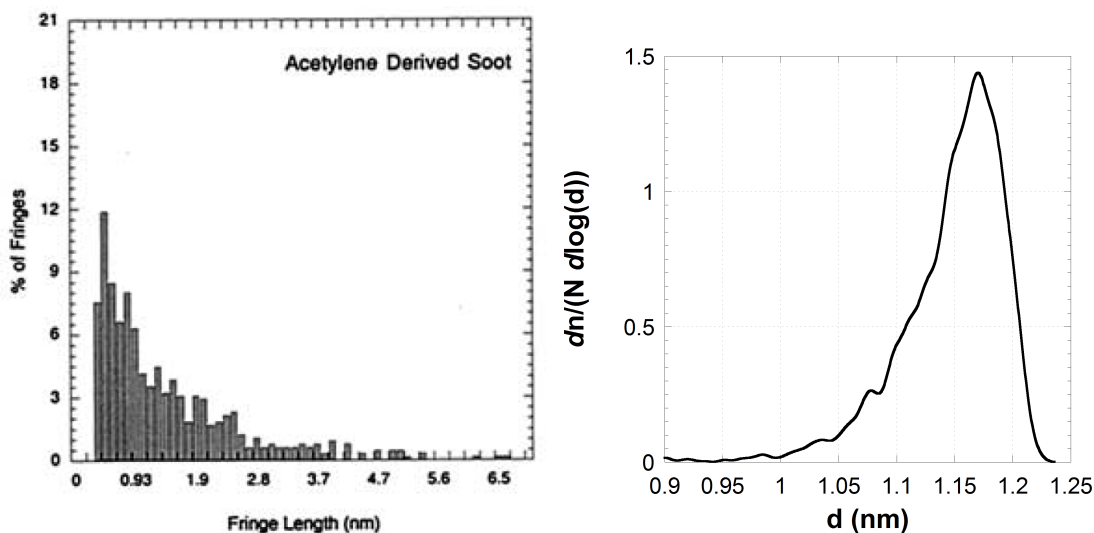


**Figure 13:** Average PAH diameter distributions. Left plot is reproduced from Vander Wal and Tomasek [29] and is for a premixed acetylene flame. Right plot was generated using the ARS model for the Kronholm reactor.

[14]. This position is further supported by the far larger free-edge growth rate compared to armchair growth. It is observed that free-edge site density starts lower than the ABF site density, but then becomes larger at later flow times. Armchair site density is substantially lower than the ABF site density.

The ARS model allows the rates of  $C_2H_2$  addition at different PAH sites to be compared. Figure 15 shows the growth rates at edges, armchairs and zig-zags. The bold curve shows the acetylene addition rate predicted by the ABF model. The free-edge growth rate appears around 6-8 times larger than the armchair rate. However, for a single site the rate of armchair growth should be faster, therefore the supposition is that this rate difference is due to the smaller concentration of armchairs in the system. Again this has been qualitatively supported by KMC simulations of single PAH structures, which show zig-zag edges are far more common than armchair edges. This is an important result which deserves further investigation. The ABF rate is greater than all ARS rates for most of the simulation. The free-edge growth rate eventually becomes greater than the ABF rate, but this may be due to the lack of a site aging parameter in the ARS model which would arrest free-edge growth. The ABF rate is calculated under the assumption of an armchair dominated surface, but this has been shown to be inaccurate.

## 7 Conclusions

The aim of this work was to advance our understanding of the chemical models which describe the fundamental processes of soot formation. A model for soot growth has been presented which builds on the basic ABF model [2]. A comprehensive reaction mecha-

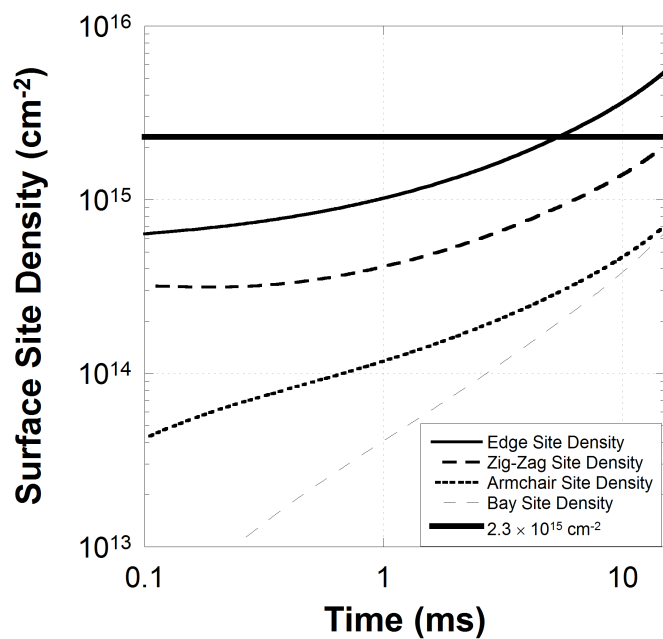


Figure 14: PAH site counts (top) and growth rates at different sites (bottom).

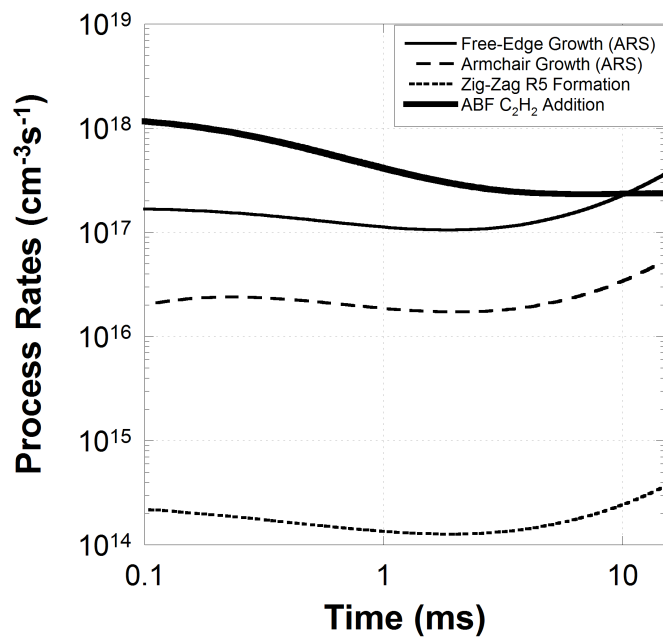


Figure 15: PAH site counts (top) and growth rates at different sites (bottom).

nism has been developed which is based on the growth of PAHs from the literature. Additionally an advanced soot particle description has been developed in order to maximise the potential of this algorithm and to eliminate some of the fixed parameters in previous models. Previously [8, 14] such comprehensive soot chemistry models have only been used to simulate the growth of single PAH molecules, which cannot give insight into the dynamics of complete systems. For the first time this has been possible with the compilation of this mechanism and the development of the site-counting model in this work.

The advanced soot model and particle description developed in this work was compared to the standard ABF model by simulated a plug-flow reactor. The plug-flow reactor has a simple geometry that can be approximated by a batch reactor model and therefore was suitable for coupling using the Strang splitting method described previously. Predictions of bulk properties of soot mass concentration and average particle diameter were compared to experimental results. Both models gave a reasonable prediction when using a surface-volume model [24] to give an approximation of soot aggregate structure. However, the new model achieved a better prediction of both quantities. A study of carbon to hydrogen ratio in soot particles in the PFR was presented for the which demonstrated that the model predicts C/H ratio to increase over time and that larger particles occupy a narrower range of compositions. Predicted C/H ratios were in agreement with those suggested by other work for young soot particles [30].

The ARS model was also capable of predicting the average size of PAHs in soot particles, albeit compared to data for a premixed flame. This comparison is very encouraging as it demonstrates that the model is able to predict a wide range of experimentally observed properties.

## References

- [1] G L Agafonov, I Naydenova, P A Vlasov, and J Warnatz. Detailed kinetic modeling of soot formation in shock tube pyrolysis and oxidation of toluene and n-heptane. *Proc. Combust. Inst.*, 31(1):575–583, 2007. doi:10.1016/j.proci.2006.07.191.
- [2] Jörg Appel, Henning Bockhorn, and Michael Frenklach. Kinetic modeling of soot formation with detailed chemistry and physics: Laminar premixed flames of C<sub>2</sub> hydrocarbons. *Combust. Flame*, 121:122–136, 2000. doi:10.1016/S0010-2180(99)00135-2.
- [3] Jörg Appel, Henning Bockhorn, and Michael Wulkow. A detailed numerical study of the evolution of soot particle size distributions in laminar premixed flames. *Chemosphere*, 42:635–645, 2001. doi:10.1016/S0045-6535(00)00237-X.
- [4] M Balthasar and M Kraft. A stochastic approach to solve the particle size distribution function of soot particles in laminar premixed flames. *Combust. Flame*, 133:289–298, 2003. doi:10.1016/S0010-2180(03)00003-8.
- [5] Michael Balthasar and Michael Frenklach. Monte-Carlo simulation of soot particle coagulation and aggregation: The effect of a realistic size distribution. *Proc. Combust. Inst.*, 30:1467–1475, 2005. doi:10.1016/j.proci.2004.07.035.
- [6] Matthew S Celnik, Robert I A Patterson, Markus Kraft, and Wolfgang Wagner. Coupling a stochastic soot population balance to gas-phase chemistry using operator splitting. *Combust. Flame*, 148(3):158–176, 2007. doi:10.1016/j.combustflame.2006.10.007.
- [7] Pascal de Sainte Claire, Philippe Barbarat, and William L Hase. *Ab Initio* potential and variational transition state theory rate constant for H-atom association with the diamond (111) surface. *J. Chem. Phys.*, 101(3):2476–2488, 1994. doi:10.1063/1.467687.
- [8] Michael Frenklach. On surface growth mechanism of soot particles. *Proc. Combust. Inst.*, 26:2285–2293, 1996. doi:10.1016/S0082-0784(96)80056-7.
- [9] Michael Frenklach. Method of moments with interpolative closure. *Chem. Eng. Sci.*, 57:2229–2239, 2002. doi:10.1016/S0009-2509(02)00113-6.
- [10] Michael Frenklach and Jonathan Ping. On the role of surface migration in the growth and structure of graphene layers. *Carbon*, 42:1209–1212, 2004. doi:10.1016/j.carbon.2004.01.025.
- [11] Michael Frenklach and Hai Wang. Detailed modeling of soot particle nucleation and growth. *Proc. Combust. Inst.*, 23:1559–1566, 1990. doi:10.1016/S0082-0784(06)80426-1.
- [12] Michael Frenklach and Hai Wang. *Detailed Mechanism and Modelling of Soot Particle Formation*, volume 59 of *Series in Chemical Physics*, pages 162–190. Springer Verlag, Berlin, 1994. ISBN 354058398X 9783540583981.

- [13] Michael Frenklach, Nigel W Moriarty, and Nancy J Brown. Hydrogen migration in polyaromatic growth. *Proc. Combust. Inst.*, 27(2):1655–1661, 1998. doi:10.1016/S0082-0784(98)80004-0.
- [14] Michael Frenklach, Charles A Schuetz, and Jonathan Ping. Migration mechanism of aromatic-edge growth. *Proc. Combust. Inst.*, 30:1389–1396, 2005. doi:10.1016/j.proci.2004.07.048.
- [15] Stephen J Harris and Anita M Weiner. Chemical kinetics of soot particle growth. *Ann. Rev. Phys. Chem.*, 36:31–52, 1985. doi:10.1146/annurev.pc.36.100185.000335.
- [16] K H Homann. Carbon formation in premixed flames. *Combust. Flame*, 11(4):265–287, 1967. doi:10.1016/0010-2180(67)90017-X.
- [17] A Kazakov and M Frenklach. Dynamic modeling of soot particle coagulation and aggregation: Implementation with the method of moments and application to high-pressure laminar premixed flames. *Combust. Flame*, 114:484–501, 1998. doi:10.1016/S0010-2180(97)00322-2.
- [18] A Kazakov, H Wang, and M Frenklach. Detailed modeling of soot formation in laminar premixed ethylene flames at a pressure of 10 bar. *Combust. Flame*, 100:111–120, 1995. doi:10.1016/0010-2180(94)00086-8.
- [19] David F Kronholm and Jack B Howard. Analysis of soot surface growth pathways using published PFR data with new PSD measurements and published premixed flame data. *Proc. Combust. Inst.*, 28:2555–2561, 2000. doi:10.1016/S0082-0784(00)80672-4.
- [20] David Franklin Kronholm. *Molecular Growth Pathways in Fuel-Rich Combustion*. PhD thesis, Massachusetts Institute of Technology, 2000.
- [21] Frederick W Lam, Jack B Howard, and John P Longwell. The behaviour of polycyclic aromatic hydrocarbons during the early stages of soot formation. *Proc. Combust. Inst.*, 22:323–332, 1989. doi:10.1016/S0082-0784(89)80038-4.
- [22] J A Marr. *PAH chemistry in a jet-stirred/plug-flow reactor system*. PhD thesis, Massachusetts Institute of Technology, 1993.
- [23] Neal Morgan, Markus Kraft, Michael Balthasar, David Wong, Michael Frenklach, and Pablo Mitchell. Numerical simulations of soot aggregation in premixed laminar flames. *Proc. Combust. Inst.*, 31:693–700, 2007. doi:10.1016/j.proci.2006.08.021.
- [24] Robert I A Patterson and Markus Kraft. Models for the aggregate structure of soot particles. *Combust. Flame*, 151:160–172, 2007. doi:10.1016/j.combustflame.2007.04.012.
- [25] Robert I A Patterson, Jasdeep Singh, Michael Balthasar, Markus Kraft, and Wolfgang Wagner. Extending stochastic soot simulation to higher pressures. *Combust. Flame*, 145(3):638–642, 2006. doi:10.1016/j.combustflame.2006.02.005.

- [26] Henning Richter and Jack Howard. Formation and consumption of single-ring aromatic hydrocarbons and their precursors in premixed acetylene, ethylene and benzene flames. *Phys. Chem. Chem. Phys.*, 4:2038–2055, 2002. doi:10.1039/b110089k.
- [27] Henning Richter, Silvia Granata, William H Green, and Jack B Howard. Detailed modelling of PAH and soot formation in a laminar premixed benzene/oxygen/argon low-pressure flame. *Proc. Combust. Inst.*, 30:1397–1405, 2005. doi:10.1016/j.proci.2004.08.088.
- [28] J Singh, R I A Patterson, M Balthasar, M Kraft, and W Wagner. Modelling soot particle size distribution: Dynamics of pressure regimes. Technical Report 25, c4e Preprint-Series, Cambridge, 2004. URL <http://como.cheng.cam.ac.uk>. Material from this preprint has been published in Patterson et al. [25].
- [29] Randall L Vander Wal and Aaron J Tomasek. Soot oxidation: dependence upon initial nanostructure. *Combust. Flame*, 134:1–9, 2002. doi:10.1016/S0010-2180(03)00084-1.
- [30] Angela Violi. Modeling of soot particle inception in aromatic and aliphatic premixed flames. *Combust. Flame*, 139:279–287, 2004. doi:10.1016/j.combustflame.2004.08.013.
- [31] Angela Violi and Sergei Izvekov. Soot primary particle formulation from multiscale coarse-grained molecular dynamics simulation. *Proc. Combust. Inst.*, 31:529–537, 2007. doi:10.1016/j.proci.2006.07.240.
- [32] Hai Wang and Michael Frenklach. Calculations of rate coefficients for the chemically activated reactions of acetylene with vinylic and aromatic radicals. *J. Phys. Chem.*, 98(44):11465–11489, 1994. doi:10.1021/j100095a033.
- [33] Hai Wang and Michael Frenklach. A detailed kinetic modeling study of aromatic formation in laminar premixed acetylene and ethylene flames. *Combust. Flame*, 110:173–221, 1997. doi:10.1016/S0010-2180(97)00068-0.
- [34] John Z Wen, M J Thomson, S H Park, S N Rogak, and M F Lightstone. Study of soot growth in a plug flow reactor using a moving sectional model. *Proc. Combust. Inst.*, 30(1):1477–1484, 2005. doi:10.1016/j.proci.2004.08.178.



**Table 3:** Changes to particle state due to jump processes in table 2 <sup>a</sup>

Process	C	H	N <sub>ed</sub>	N <sub>zz</sub>	N <sub>ac</sub>	N <sub>bay</sub>	N <sub>R5</sub>	N <sub>PAH</sub>	Inc. <sup>b</sup>	Dec. <sup>c</sup>
<b>Inception Processes</b>										
Pyrene inception	32	20	12	8	0	0	0	2	.	.
<b>Surface Processes</b>										
S1 Free-edge ring growth	+4	+2	+2	.	.	.	.	.	2	.
S2 Free-edge ring desorption	-4	-2	-2	.	.	.	.	.	.	2
S3 R5 addition	+2	.	.	-1	.	.	+1	.	.	.
S4 R5 desorption	-2	.	.	+1	.	.	-1	.	.	.
S5 Armchair ring growth	+2	.	+1	.	-1	.	.	.	2	.
S6 R5-R6 conversion at free-edge	+2	+2	+2	.	+1	.	-1	.	1	.
S7 R6-R5 conversion at free-edge	-2	-2	-2	.	-1	.	+1	.	.	1
S8 R5-R6 conversion at armchair	.	.	+1	.	.	.	-1	.	1	.
<b>PAH Condensation Processes</b>										
Pyrene condensation	+16	+10	+6	+4	.	.	.	+1	.	.
<b>Oxidation Processes</b>										
S9 Free-edge O <sub>2</sub> oxidation	-4	-2	-2	.	.	.	.	.	.	2
S10 Free-edge OH oxidation	-4	-2	-2	.	.	.	.	.	.	2
S11 Armchair O <sub>2</sub> oxidation	-2	.	-1	.	+1	.	.	.	.	2
S12 Armchair OH oxidation	-2	.	-1	.	+1	.	.	.	.	2

<sup>a</sup>Surface area is updated according to the surface-volume model of Patterson and Kraft [24].

<sup>b</sup>Increment number of uniformly chosen sites according to table 5(a).

<sup>c</sup>Decrement number of uniformly chosen sites according to table 5(b).

**Table 4:** Neighbouring site probability weight distributions for each stochastic process.

Process	Site	$P_{ed}$	$P_{zz}$	$P_{ac}$	$P_{bay}$
S1 Free-edge growth	Free-edge	0.10	0.27	0.40	0.23
S2 Free-edge desorption	R6	0.00	0.05	0.61	0.34
S3 R5 addition	Zig-zag	N/A			
S4 R5 desorption	R5	N/A			
S5 Armchair growth	Armchair	0.68	0.20	0.04	0.08
S6 R5 free-edge conversion	ED-R5	0.25	0.25	0.25	0.25
S7 R5 free-edge desorption	AC-R6	0.00	0.06	0.57	0.37
S8 R5 armchair conversion	AC-R5	0.25	0.25	0.25	0.25
S9 O <sub>2</sub> free-edge oxidation	R6	0.00	0.32	0.39	0.29
S10 OH free-edge oxidation	R6	0.00	0.36	0.41	0.23
S11 O <sub>2</sub> armchair oxidation	Armchair	0.00	0.08	0.53	0.39
S12 OH armchair oxidation	Armchair	0.00	0.08	0.38	0.54

**Table 5:** Particle state changes when incrementing sites. Reverse signs for decrementing changes.

(a) Site Incrementing

Original Site	$N_{ed}$	$N_{zz}$	$N_{ac}$	$N_{bay}$	$N_{R5}$
Free-edge	-1	+1	.	.	.
Zig-zag	.	-1	+1	.	.
Armchair	.	.	-1	+1	.
Hole	.	.	.	-1	.

(b) Site Decrementing

Original Site	$N_{ed}$	$N_{zz}$	$N_{ac}$	$N_{bay}$	$N_{R5}$
Zig-zag	+1	-1	.	.	.
Armchair	.	+1	-1	.	.
Hole	.	.	+1	-1	.